PAPER • **OPEN ACCESS**

Absolute neutron emission estimate on MAST Upgrade based on activation foil measurements

OPEN ACCESS
IOP Publishing
Plasma Physics and Controlled Fusion
Plasma Phys. Control. Fusion **67** (2025) 065011 (12pp)
https://doi.org/10.1088/1361-6587/add764

Absolute neutron emission estimate on MAST Upgrade based on activation foil measurements

C L MacLean[1,*], M Cecconello[1,2], S Allan[3], C L Grove[3], R Worrall[3], K Lennon[3,4], the MAST Upgrade Team[5] and the EUROfusion Tokamak Exploitation Team[6]

[1] Department of Physics, University of Durham, Durham DH1 3LS, United Kingdom
[2] Department of Physics and Astronomy, Uppsala University, Uppsala SE-75105, Sweden
[3] United Kingdom Atomic Energy Authority, Culham Campus, Abingdon, Oxon OX14 3DB, United Kingdom
[4] Materials and Engineering Research Institute, Sheffield Hallam University, Howard Street, Sheffield S1 1WB, United Kingdom

E-mail: craig.l.maclean@durham.ac.uk

Received 20 September 2024, revised 13 April 2025
Accepted for publication 12 May 2025
Published 21 May 2025

Abstract

Determination of the absolute neutron rate production in any fusion device and in particular for ITER and future power plants is essential for their operation and for the optimization of the fusion power. A common calibration approach is to use well characterized neutron sources placed inside the vacuum vessel combined with Monte Carlo simulations. This method is fraught with several difficulties both from an engineering and data modeling and interpretation point of view. This is particularly true for future fusion power plants. This work demonstrates an alternative approach to the absolute calibration of the neutron rate based on activation foil measurements combined with forward modeling of a well characterized plasma discharge and fusion device. This method has been applied to MAST Upgrade and the good agreement found between measured and modeled foil activity support this approach. The results presented suffer from some limitations but suggestions are given on how to resolve them.

Keywords: fusion, diagnostics, neutronics, modelling, activation foil, MAST-U, MAST Upgrade

1. Introduction

Absolute calibration of neutron diagnostics is fundamental for the safe operation of present day devices and future power plant reactors and for the estimates of the total fusion power. The most commonly used approach is to monitor the neutron emission with an absolutely calibrated Fission Chamber (FC) using a strong neutron source with a well characterized neutron emission spectrum placed at different locations inside the vacuum vessel [1–9]. Neutron transport Monte Carlo codes are then used to model the neutron source, the tokamak and its environment and the FC thus providing the relationship between the neutron source strength and the measured flux at the absolutely calibrated FC [10, 11]. This method, however, is technologically quite complex and time consuming (with long shut-down periods) requiring very strong neutron sources with the associated complications for their safe handling. In addition, periodic calibrations are required to track changes in the calibration factors. Activation foil

[5] See Harrison *et al* 2019 (https://doi.org/10.1088/1741-4326/ab121c) for the MAST Upgrade Team.
[6] See Joffrin *et al* 2024 (https://doi.org/10.1088/1741-4326/ad2be4) for the EUROfusion Tokamak Exploitation Team.
[*] Author to whom any correspondence should be addressed.

measurements are often used as additional benchmarks of this calibration method and good agreement between the two has been reported extensively in literature [12–16]. An alternative approach is the use of well characterized plasma discharges as the neutron source in combination with neutron activation foils (AFs), located in the proximity of the plasma. The neutron source is modeled by codes such as TRANSP/NUBEAM [17, 18] while the total neutron flux at the AF location which includes scattered neutrons is calculated via neutron transport Monte Carlo codes. Agreement between predicted and observed activation is then used to confirm the correctness of the modeling and to provide the absolute calibration factors for the fission chambers. Although this approach is also based on neutron transport calculation, the modeling effort is quite reduced if the AFs are placed inside the vacuum vessel and as close as possible to the neutron source. This also ensures that the total neutron flux at the AF locations is not significantly affected by changes in the environment outside the tokamak which is not uncommon during the typical life-time of a fusion device. This second approach to the absolute neutron calibration as applied to MAST Upgrade is described in this work.

MAST Upgrade is a spherical tokamak with a small aspect ratio $R/a \approx 0.85/0.65 \approx 1.3$ operated with low magnetic field (typically between 0.4 and 0.7 T) and plasma currents in the range 0.5–1.0 MA. External auxiliary heating is currently provided by two neutral beam injection (NBI) systems delivering up to 3.5 MW of heating power by injecting deuterons with energies up to 70 keV (two additional NBIs are planned to be installed in the near future). Neutron emission on MAST Upgrade is entirely dominated by the beam-thermal ($\approx 85\%$) and beam–beam ($\approx 15\%$) fusion reactions with the thermal contribution being negligible. MAST Upgrade is equipped with three neutron diagnostics: a set of two fission chambers located outside and in close proximity to the vacuum vessel, an absolutely calibrated neutron camera (NCU, [19, 20]) and three AF stations. While the fission chambers and the neutron camera are standard diagnostics and are regularly available, the activation stations are used only on a limited number of experimental dates.

Section 2 details the properties of the activation stations, of the AFs and of the γ-ray detectors used to measure the activity as well as the experimental dates on which AF measurements were collected. The modeling of the neutron flux at the AF locations and expected number of counts on the γ-ray detectors for these experimental dates are presented in section 3 together with the error analysis. The comparison between predicted and measured counts and the implications for the absolute calibration of fission chambers is discussed in section 4 where also the conclusions are drawn.

2. Experimental setup

MAST Upgrade three AF stations are located in sectors 5, 10 and 12 at $(R,Z) = (202, -11)$ cm, $(R,Z) = (202, -21)$ cm and $(R,Z) = (202, 10)$ cm respectively. Each station consists of a re-entrant pipe mounted on an equatorial flange and separated by the vacuum chamber by a thin wall of 0.7 mm thickness to reduce the absorption and scattering of neutrons. Only one foil can be housed in each station, but multiple stations can be used per experimental day. A CAD view of activation stations at sectors 5 and 12 is shown in figure 1 while the left panel of figure 2 shows their toroidal location. The AF disks are placed inside a hollow plastic cylinder which is manually inserted into the re-entrant pipe (see right panel of figure 2) at the beginning of each experimental day.

Four identical Indium disks were used each with a diameter of 25 mm and a thickness of 4 mm with an assumed natural isotopic fraction of 95.71% for ^{115}In and 4.29% for ^{113}In (no certification was available). Activation foil measurements were carried out parasitically on a number of experimental days, listed in table 1, during the first three MAST Upgrade scientific campaigns (indicated as MU01, MU02, and MU03 respectively). These consisted of a large variety of (*i*) plasma scenarios with currents ranging from 0.6 to 1.0 MA in L- or H-mode, (*ii*) NBI heating timing and combinations (on-axis only, off-axis only or both), (*iii*) plasma density and temperature, (*iv*) equilibria (single- and double-null conventional divertor or Super-X divertor), (*v*) MHD instabilities (sawteeth, TAEs, fish-bones, Long-Lived Mode, Neoclassical Tearing Modes, ELMs, Internal Reconnection Events) and (*vi*) ELM controls mechanisms. As a result, the spatial distribution and time evolution of the neutron emissivity varied significantly: figure 3 is an example of this. The AFs were inserted prior to the first plasma discharge of each experimental day and removed after the last one. The start time of the irradiation sequence was set to zero when the first NBI heating was applied and subsequently the start and duration of each NBI heating were accurately recorded.

Post-irradiation, the activity was measured through γ-ray spectrometry on the same day as activation for 24 h (with the exception of 15 October 2021, see note (†) in table 1) with the start and end time of the measurement phase being accurately recorded. Two absolutely calibrated γ-ray detectors were used: a Broad Energy High-Purity Germanium HPGe BE3825 (BEGe) and a Single Anode Germanium (SAGe) well-type detector with the same experimental setup for all measurements with the exception of 28 October 2021 for which the distance between AF and γ-ray detector was different (see note (‡) in table 1). Data acquisition was carried out via a Lynx digital MCA device connected to a PC with Genie2000 software for analysis. An energy calibration and efficiency check were carried out with a mixed radionuclide source of known activity for each experimental day and background radiation checks were regularly done to ensure that the measurements were not contaminated by unwanted radiation sources. The typical dead-time observed during the activation measurements was less than 0.3% of the counting time. The activated nuclide of interest is the meta-stable state of ^{115m}In with half-life of 4.49 hours which, after irradiation, emits a γ-ray with energy $E_\gamma = 336$ keV together with several delayed γ-rays from induced neutron capture in the AF. Also present in the gamma spectrum are γ-rays from other indium activation products, which are unimportant to this project. The absolute efficiency ϵ at $E_\gamma = 336$ keV is $0.0742 \pm 8\%$ and $0.0539 \pm 8\%$

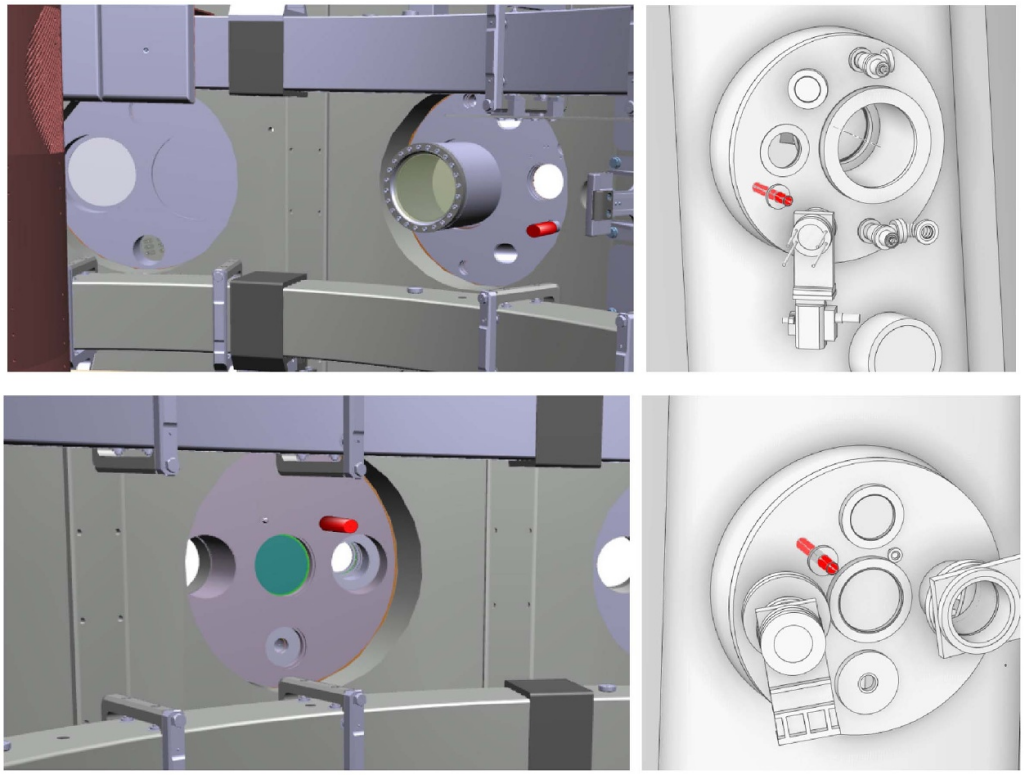

Figure 1. CAD view of the activation foil stations (in red) in sectors 5 (top) and 12 (bottom) on the equatorial flanges from the inside/outside of the vacuum vessel (on the left/right respectively). Clearly visible in the view from the inside are the P5 upper and lower poloidal field coils.

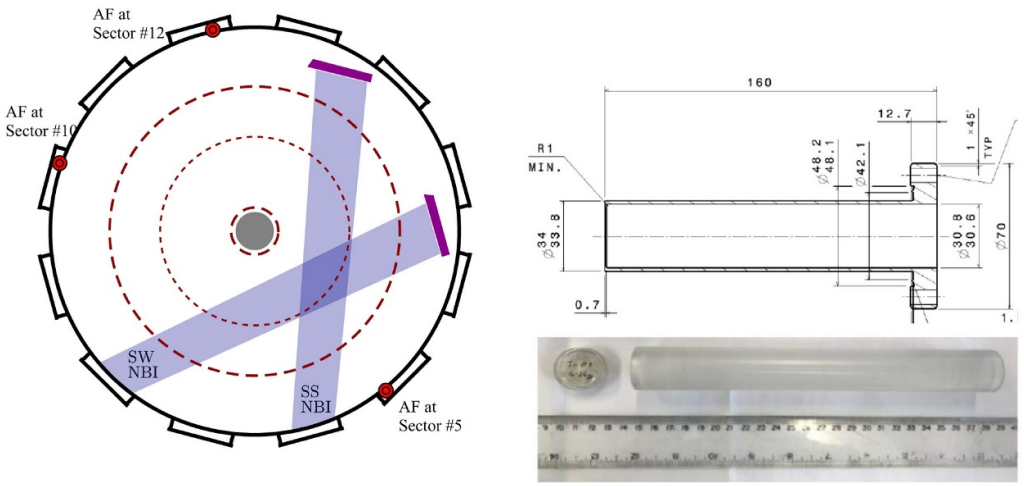

Figure 2. Left: toroidal location of the AF stations (red circles) as viewed from the top (dashed lines indicates LCFS and magnetic axis); also shown are the footprints of the two NBIs. Right: CAD cross-section of an activation foil re-entrant flange (top) and a photo of the activation foil with plastic sleeve for insertion and removal.

for the BEGe and SAGe detectors respectively. This has been estimated numerically using the Canberra LabSOCS software [21] which is based on the simulation of the γ-ray energy spectrum for a known source and detector combination using the Monte Carlo transport code MCNP [22] verified against known measurements. An example of the γ-ray energy spectrum emitted by the activated In foil after the exposure to MAST-U on the 08 October 2021 is shown in figure 4 with the insert showing the photo-peak of the 336.24 keV γ-ray emitted by the first meta-stable In foil. The red area represents the actual counts with the radiation background subtracted. The specific activity, the neutron fluence measured by the fission chamber and the total neutron counts measured by the neutron camera (the integral of the sum of the count rates in

Table 1. Complete list of the AF measurements carried out during the MAST Upgrade experimental campaigns MU01 to MU03. Columns: γ-ray detector (B for BEGe, S for SAGe); fission chamber fluence; experimentally measured number of decays (also referred to as peak area) N_E and specific activity A_S after each experimental day and total number of counts on the Neutron Camera Upgrade (NCU). Notes: (†) 30 min measurement instead of 24 hr; (‡) different γ-ray detector geometry.

Exp.	Date	Sector /AF	γ	Yield ($\times 10^{14}$)	N_E ($\times 10^5$)	A_S (Bq/g)	NCU ($\times 10^6$)	Pulse numbers
MU01	08 October 2021	12/7	B	1.02	1.740	15 ± 1	1.45	45 212–45 221
(†)	15 October 2021	12/7	B	1.50	0.154	18 ± 1	—	45 301–45 316
	22 October 2021	12/6	B	2.12	3.227	29 ± 2	2.98	45 389–45 403
(‡)	28 October 2021	12/7	B	1.30	0.137	18 ± 1	1.75	45 474, 45 483
MU02	26 January 2023	12/4	B	1.99	2.942	28 ± 3	3.05	47 078–47 097
	27 January 2023	12/7	B	1.90	1.952	26 ± 2	—	47 101–47 119
MU03	20 October 2023	5/7	B	1.44	2.196	25 ± 2	2.03	48 543–48 547
		12/8	S		1.541	25 ± 2		
	27 October 2023	5/4	B	3.36	4.026	42 ± 3	5.02	48 607–48 624
		12/8	S		2.786	42 ± 3		
	19 December 2023	12/8	B	2.76	3.001	30 ± 2	—	49 185–49 202
		5/7	S		2.928	42 ± 3		
	18 January 2024	5/7	B	3.23	3.749	40 ± 3	4.85	49 361–49 380
		12/8	S		3.678	57 ± 5		

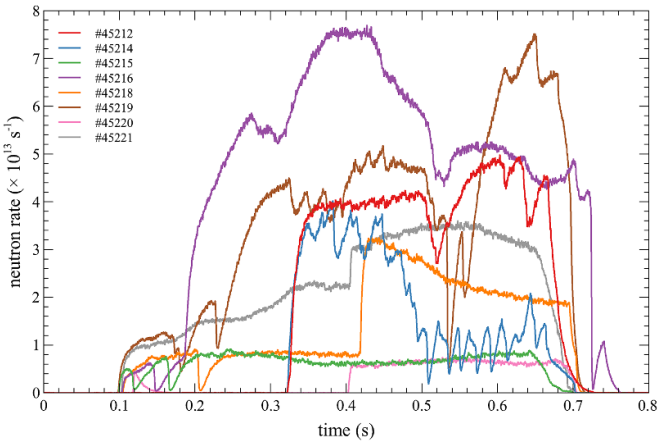

Figure 3. Time evolution of the neutron rate measured by the fission chamber for the activation foil measurement on the 08-10-2021.

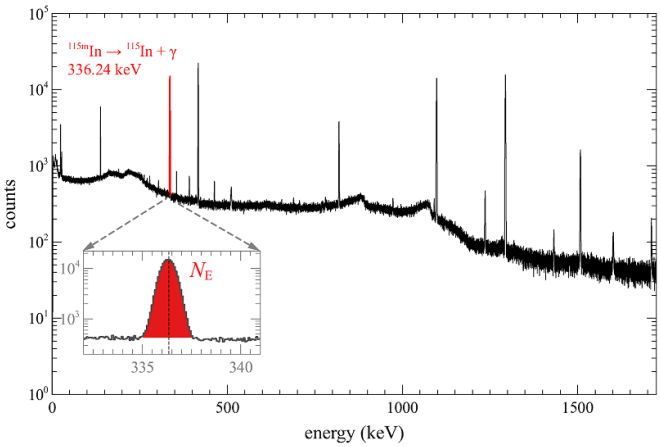

Figure 4. Energy spectra collected for 24 h using the BEGe detector of the activation foil 7 in sector 12 after its exposure to MAST-U plasmas on the 08 October 2021. The red peak corresponds to experimental counts N_E of the 336 keV gammas produced from the decay of activated ^{115m}In. All other peaks in the spectrum are due to γ-ray emission from other indium activation products, such as ^{116m}In.

each of the six lines of sight) are reported in table 1. Neutron camera data were not available for all the activation measurements as indicated in the table. The relationship between the neutron fluence and the specific activity is shown in the left panel of figure 5: although roughly proportional to each other, there are some large deviations from a purely linear relationship. The right panel of the same figure shows the relationship between the neutron fluence as measured by the fission chamber and the total neutron counts obtained from the NCU: the very good linear relationship between the two indicates that the large deviations from the expected linearity in the case of the specific activity can not be attributed to problems in the fission chamber. Note that the NCU is absolutely calibrated while the fission chamber is not. Instead the FC has been matched to TRANSP/NUBEAM predictions in selected plasma scenarios characterized by no fast ion losses or redistribution as inferred from the absence of the typical signature in the OMAHA Mirnov pick-up coils of MHD instabilities such as TAEs, FBs, LLMs, sawteeth and ELMs. A detailed analysis of the AF measurements has shown no clear dependency on the specific foil, the measurement location (sector), the experimental campaign and the γ-ray detector used. The reason for this behavior remains unclear to date.

The FCs on MAST Upgrade are the same that were installed in MAST and were absolutely calibrated in-situ as described in the paper by Keith Stammers and M.J. Loughlin [23]. However, a recent study has shown the FC has a deficit in the measurement of fusion products when compared to both the NCU and proton detector on MAST-U [24].

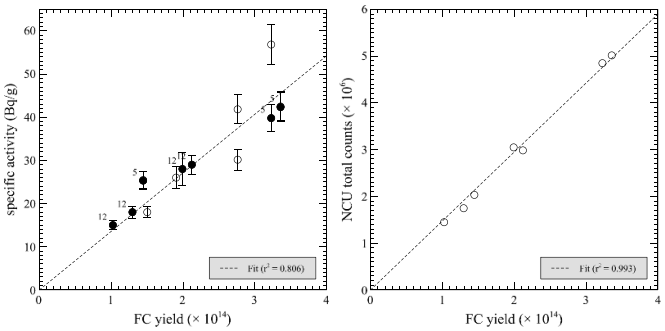

Figure 5. Scaling between the neutron yield as measured by the fission chamber and the specific activity (left panel) of the AFs for all AF experiments, and the NCU total counts (right panel) for experimental days where NCU data was available. The solid black circles on the left panel correspond to the data shown on the right panel and the sector is indicated by the number on the top left of the selected data.

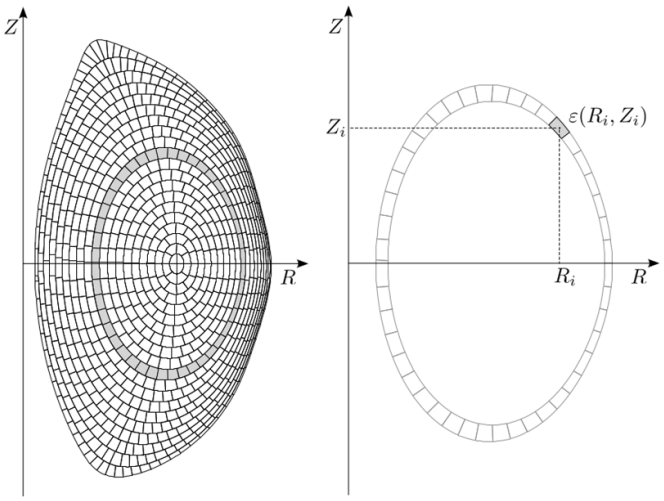

Figure 6. Left figure: geometry of the 840 toroidally axis-symmetric zones used in TRANSP/NUBEAM in which the neutron emissivity ε is calculated for a typical MAST Upgrade equilibrium. The shaded region corresponds to the zones for a specific flux surface and it is shown in detail on the right where a single zone located at (R_i, Z_i) is shown with its non-flux averaged neutron emissivity $\varepsilon(R_i, Z_i)$.

3. Modeling of the induced activity in the indium foil

Modeling of the induced activity in the indium foils requires the estimation of the neutron flux on the foil including both the direct and scattered neutron contributions during each plasma discharge, the modeling of the irradiation and decay sequence for the entire exposure day and the modeling of the detection of the γ-ray during the activity measurements. This will provide the predicted number of counts expected in the 336 keV γ-ray peak which will then be compared to the experimental observations reported in table 1. The neutron emissivity is calculated using the TRANSP/NUBEAM codes to estimate the direct neutron component and the MCNP code for the scattered one: these two steps are detailed in sections 3.1 and 3.2 respectively. The neutron flux at the AF is calculated as described in section 3.3. Modeling of the irradiation and decay sequence and the expected γ-ray counts in the detector are described in section 3.4. Given the complexity of the steps involved only a limited number of days per experimental campaign were selected for the complete modeling: 08 October 2021 for MU01, 20 October 2023 and 27 October 2023 for MU03 and both days for MU02. The reason for selecting these dates is that they provide a good representation of the spread in the experimentally measured specific activity around the expected linear relation.

3.1. TRANSP/NUBEAM modeling of the direct neutron emissivity

Each plasma discharge (indicated by the index q) has been modeled in TRANSP/NUBEAM using an externally imposed equilibrium calculated by EFIT++ [25, 26] constrained, whenever available, by measurements of the current density obtained via the motional Stark effect diagnostic [27]. Kinetic profiles were provided by the Thomson scattering diagnostic [28], while plasma rotation was from the CXRS spectroscopic diagnostic. No $Z_{\rm eff}$ measurement is available on MAST Upgrade and it was assumed to have a constant profile with the value of $Z_{\rm eff} = 1.5$ [29, 30]. The fast ion distribution has been calculated by NUBEAM with high statistics including the correction for finite Larmor effects to account for the guiding-centre approximation in the calculation of the fast ion orbits. The NBIs energy fractions were set to their nominal values (0.70/0.19/0.11 for on-axis, 0.78/0.16/0.06 for off-axis) with the exclusion of the on-axis NBI during MU01 which was set to 0.4/0.4/0.2 as inferred from spectroscopic measurements: this was due to an improper set-up of the magnets in the NBI ionization source that was rectified at the end of MU01. The non-flux averaged neutron emissivity has been calculated in 5 ms intervals at M time points during the flat-top phase of each plasma discharge q. The non-flux averaged neutron emissivity is a more realistic representation of the neutron emissivity taking into account poloidal asymmetries that are neglected in the standard TRANSP/NUBEAM output. The non-flux averaged neutron emissivity is calculated on an 2D irregular grid consisting of $I = 840$ points of coordinates (R_i, Z_i) to which a toroidal volume V_i and neutron emissivity ε_i are associated as shown in figure 6. Toroidal field ripples have a negligible effect on the confinement of fast ions [31] and they have not been included in the modeling. The reduced fast ion confinement due to MHD instabilities such as internal reconnection events, sawteeth, TAEs, fish-bones, ELMS and to mode-locking can result in a significant reduction in the neutron emissivity and consequently of the neutron flux reaching the AF. The TRANSP/NUBEAM simplified models for sawtooth and fish-bones and the anomalous fast ion diffusion coefficient for the heuristic description of the effect of TAEs and LLMs [32] have not been used in these simulations: the need for an ad-hoc adjustment of the several parameters in such models for each plasma discharge made this approach impractical. Instead, the neutron rate predicted by TRANSP/NUBEAM is compared to the one measured by the FC (as a proportional

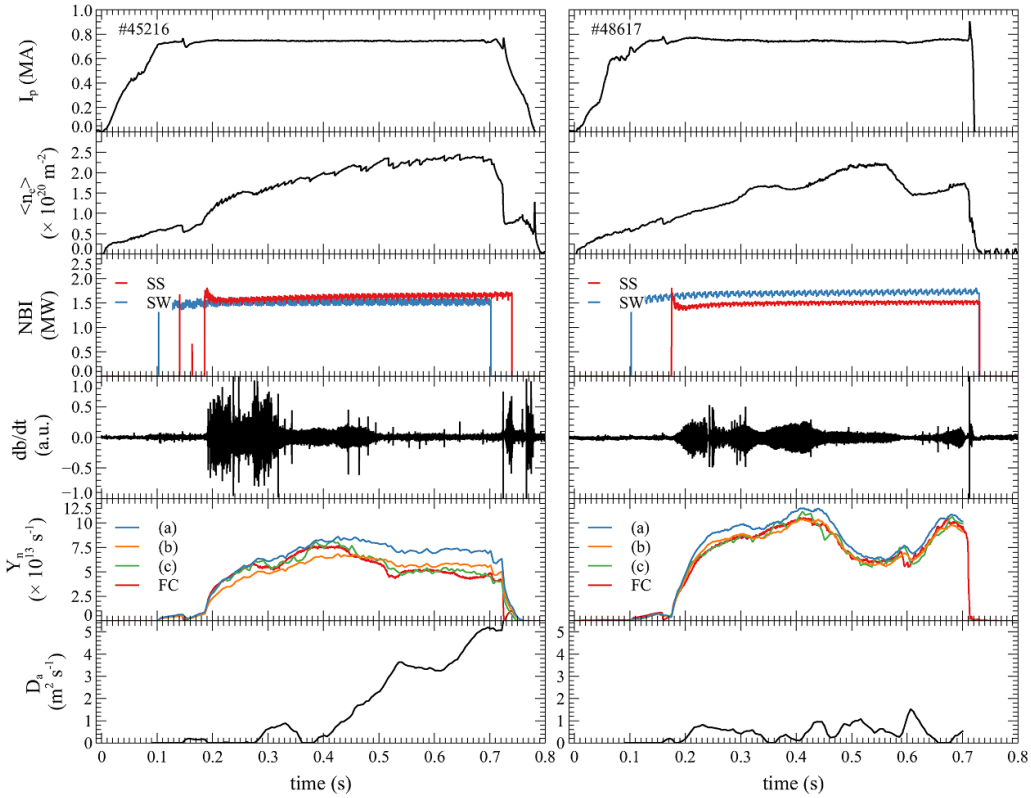

Figure 7. Plasma discharges #45216 (left) and #48617 (right). From top to bottom: plasma current, line integrated electron density, on- and off-axis NBI power (SS and SW respectively), Mirnov coil magnetic fluctuations, neutron rate from the FC (red) and TRANSP/NUBEAM and anomalous fast ion diffusion. TRANSP/NUBEAM trace in blue (a) is with $D_a = 0$ m^2 s^{-1}, in dark yellow (b) it is multiplied by the correction factors $\Gamma = 0.79$ (#45216) and $\Gamma = 0.90$ (#48617) and in green (c) is with $\max(D_a) = 10$ m^2 s^{-1}.

representation of the neutron yield) and scaled to match it: this correction factor, calculated as the ratio of the integrated neutron fluences and indicated as Γ in the remainder of the paper, is of the order of 10% for most cases, and at most 25% for a few selected cases. An example is provided in figure 7 where the time traces for plasma discharges #45216 and #48617 (see table 1) show the comparison of the two methods in the neutron yields. An IRE occurring at approximately 150 ms into discharge #45216 causes a drop in the neutron emissivity, while between 200–300 ms TAEs and between 300–500 ms LLM results in the suppression of the fast ion population; the fast ion population remains below the TRANSP/NUBEAM prediction also during the mode-locking phase (from 500 ms to the end of the pulse) resulting in a correction factor $\Gamma \approx 0.8$. The magnetic perturbations in #48617 are similar to those of #48617 but smaller resulting in a correction factor $\Gamma \approx 0.9$.

TRANSP/NUBEAM has the capability to match the predicted neutron rate Y_{TR} to the one measured by the fission chamber Y_{FC} by means of a temporally and spatially varying anomalous fast ion diffusion D_a whose value is set by a proportional and integral feedback control algorithm. The feedback scheme includes an anti-windup term to prevent the integral term from growing too large when the calculated D_a exceeds a user-defined min and max range. In its simplest implementation, the D_a radial profile is forced constant, the minimum allowable anomalous fast ion diffusion is set to $D_a = 0$ m^2 s^{-1} while the maximum D_a is set sufficiently large to avoid saturation. This approach was tested for pulse #45216, characterized by a large time varying difference between Y_{TR} and Y_{FC}, and for pulse #48617 in which this difference is smaller and time independent. Good agreement between Y_{TR} and Y_{FC} was obtained in both case by setting $\max(D_a) = 10$ m^2 s^{-1} as shown in the fifth panel of figure 7. The bottom panels show the time evolution of D_a: in both case, $D_a(t) \leqslant 5$ m^2 s^{-1}, a value that is consistent with the ones usually required in the past to match measured and simulated neutron rates [32, 33]. The calculated neutron emissivity profile in the case of $\Gamma = 1$ and with anomalous fast ion diffusion are slightly broader compares to the ones in which $\Gamma < 1$ and no anomalous fast ion diffusion: this did not change significantly the ratio between direct and scattered neutron presented in section 3.2 and therefore have little impact on the total neutron flux at the detector. In addition, the difference Y_{TR} and Y_{FC} cannot be exclusively attributed to magnetic perturbations and therefore anomalous fast ion diffusion is not always the correct approach in describing the neutron emissivity. For these two reasons, the analysis presented in this paper is based on the scaling factor Γ and not on the feedback control algorithm.

3.2. MCNP modeling of the direct and scattered neutron flux

The flux of scattered neutrons on the AFs can be significant. This is due to the positioning of the AFs, their proximity to the plasma, and them directly facing the central column. In order

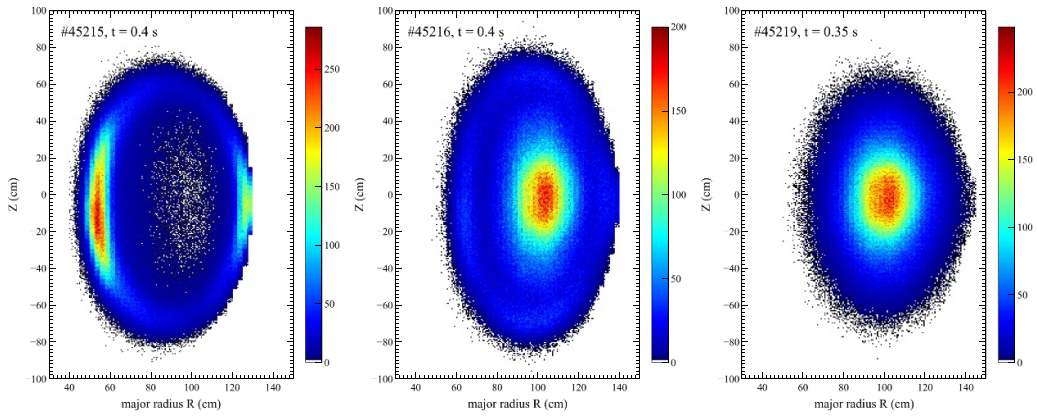

Figure 8. 2D histogram of the sampled MCNP DD neutron sources in the poloidal plane with 10^6 markers and bin area of approximately 0.5×0.5 cm^2 for off-axis NBI only (#45215), both on- and off-axis NBIs (#45216) and on-axis NBI only (#45219). The colorbar indicated the number of markers in each bin.

to estimate the contribution of scattered neutrons to the total activation of the In foil, neutron transport calculations based on the Monte Carlo code MCNP were carried out. The MCNP model used in this work is a high fidelity model of the entire experimental hall and includes, among many other components, the vacuum vessel and internals, major support structures for the vacuum vessel, the NBIs, the neutron camera, the fission chambers and the AFs, the experimental hall walls and internal fixed structures such as the mezzanine and other raised platforms, and any penetration fills in the walls. SuperMC 3.1 [34] was used to convert the CAD geometry into the MCNP geometry with high accuracy. The MCNP model does not include any equipment attached to the device which could be modified or removed, and also does not include minor components, such as the thermal blanket surrounding the vacuum vessel, within the experimental hall which offer little shielding (negligible neutron scattering sources). There is also a large quantity of wiring which is not included, primarily because its challenging to model.

Three neutron sources have been used in these simulations representative of the typical neutron emissivity for off-axis only, on-axis only and both on- and off-axis NBI heating. The neutron source spatial distribution are based on the non-flux averaged neutron emissivity for three reference discharges: plasma discharge #45215 at 0.4 s for the off-axis case, #45216 at 0.4 s for both NBIs and #45219 at 0.35 s for on-axis NBI.

For all three cases, the neutron energy distribution from DD reactions has been assumed to be Gaussian centered at 2.45 MeV with a full-width at half maximum corresponding to a temperature of 70 keV which is equal to the maximum injection energy of the NBIs in MAST-U. A 2D histogram of the spatial distribution of the MCNP neutron sources on the poloidal plane is shown in figure 8.

The calculation of the direct and scattered neutron flux energy spectra were performed for all three AF locations (sector 5, 10 and 12) in the energy range 0– 5 MeV. Functionality within MCNP has been used to filter the volume averaged flux tally (F4 type) by only recording tracks from neutrons which have not subsequently undergone an interaction, thus giving the direct neutron flux per simulated neutron Φ_{D}. The total neutron flux per simulated neutron, Φ_{T} was also calculated which, combined with the direct flux, allowed the estimation of the scattered neutrons flux $\Phi_{\mathrm{S}} = \Phi_{\mathrm{T}} - \Phi_{\mathrm{D}}$.

The histogram of the total, direct and scattered neutron fluxes in the 0–4 MeV range, in bins of 50 keV width, is shown in panels (a.1) and (b.1) of figure 9 for the AFs at sector 10 for the on-axis and off-axis only NBI cases.

The relative uncertainty in the tallies for both total and direct neutron fluxes are below 5% in the energy range 1.8–3.2 MeV. Above 3.2 MeV, an energy range that does not contribute to the calculations as shown in figure 9, the relative uncertainty in the direct and total flux increases quadratically reaching a value of 70% at 4 MeV. For energies below 1.8 MeV, the relative uncertainty in the total flux is below 5% while for the direct flux it increases quadratically to 100% at 1.35 MeV as the counts drop to zero. The results for sectors 5 and 12 are very similar to those obtained for sector 10. The broad Gaussian peak seen in figure 9 at an energy slightly below 2.45 MeV results from the superimposition of the scattered components of neutrons born with energies above 2.45 MeV.

As shown in table 2, the ratio $\int \Phi_{\mathrm{S}} \mathrm{d}E / \int \Phi_{\mathrm{D}} \mathrm{d}E$, where the integration is carried over the interval 0 to 5 MeV, is quite large for all sectors with the off-axis NBI only giving the largest values. The different components of the activation rate per simulated neutron $A = \Sigma \Phi V$, where Σ is the inelastic macroscopic cross section for the ^{115}In first meta-stable state and V its volume, has been calculated and is shown in panels (a.2) and (b.2) of figure 9. As it can be seen the contribution of scattered neutrons to the total activation is not negligible. As described in section 3.1, from TRANSP/NUBEAM it is only possible to calculate the absolute direct neutron flux ϕ_{D} at the AF (as described in section 3.3). The estimated total (direct plus scattered) neutron flux ϕ_{T} is then calculated as $\phi_{\mathrm{T}} = \kappa \phi_{\mathrm{D}}$ where the constant κ is given by $\kappa = \int \Sigma \Phi_{\mathrm{T}} \mathrm{d}E / \int \Sigma \Phi_{\mathrm{D}} \mathrm{d}E$ and is reported in the last column of table 2 for the three reference scenarios. A comparison of κ for the off-axis only and on-axis only NBI scenarios shows that the scattered

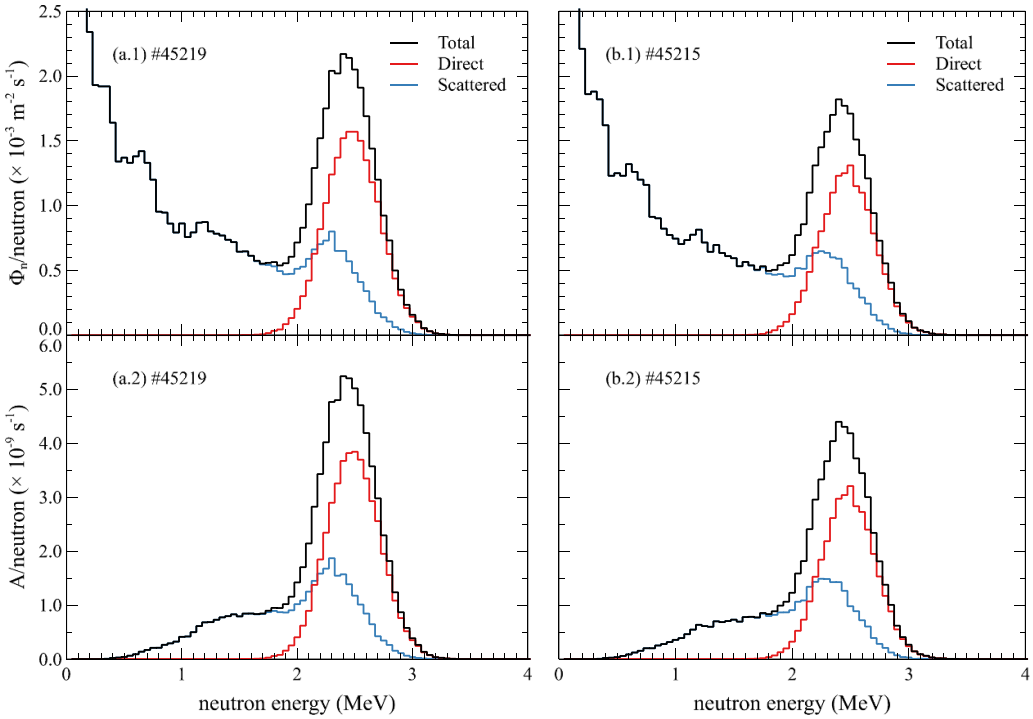

Figure 9. Total (black), direct (red) and scattered (blue) neutron fluxes per simulated neutron Φ calculated by MCNP for the activation foil at sectors 10 for on- and off-axis only NBI heating (panels a.1 and b.1 respectively). Panels (a.2) and (b.2) show the corresponding activation rate per simulated neutron $A = \Sigma\Phi_n V$ where Σ is the inelastic macroscopic cross section for the ^{115}In 1st meta-stable state and V the foil volume.

Table 2. Scattered and direct neutron flux per simulated neutron fractions estimated by MCNP at the location of the AFs in Sectors 5, 10 and 12 together with the scattered to direct ratios and the scaling factor κ for on- and off-axis NBI heating used to calculate the absolute total flux on the AFs.

Pulse	Sector	$\int \Phi_S dE / \int \Phi_T dE$	$\int \Phi_D dE / \int \Phi_T dE$	$\int \Phi_S dE / \int \Phi_D dE$	κ
45 215	5	0.77	0.23	3.43	1.81
off	10	0.79	0.21	3.78	1.92
axis	12	0.77	0.23	3.29	1.82
45 216	5	0.76	0.24	3.17	1.76
on & off	10	0.78	0.22	3.51	1.87
axis	12	0.75	0.25	3.02	1.77
45 219	5	0.75	0.25	3.00	1.74
on	10	0.76	0.24	3.20	1.81
axis	12	0.74	0.26	2.88	1.74

contribution is higher in the former as it can be expected since the source is stronger further away from the AF and closer to the central-column resulting in a larger number of scattered neutrons. The values of κ for the on-axis only and with both NBIs are more similar since the neutron emissivity due to the off-axis NBI is approximately a factor 10 smaller than the one due to the on-axis NBI. Similar estimates were carried out for the Princeton Large Torus (PLT) device where it was found that the activation by scattered neutrons was 1.24 times the one due to direct neutrons [35]. The reason for this value to be lower than the one reported here is that MAST Upgrade has a lower aspect ratio and a thinner central column ($R/a = 0.85/0.65 \approx 1.3$) compared to PLT($R/a = 1.3/0.4 \approx 3.3$). As a consequence, each point on the first wall in MAST Upgrade (and hence the AF) sees a much larger neutron source volume and scattering surface.

3.3. Total neutron flux and activation rate

For plasma discharge q, the direct neutron flux ϕ_D at the AF at time t_m is given by:

$$\phi_{D,q}(t_m) = \sum_{i=1}^{I} \sum_{j=1}^{J} \frac{n_i(t_m)}{S_{i,j}(t_m)} \quad (1)$$

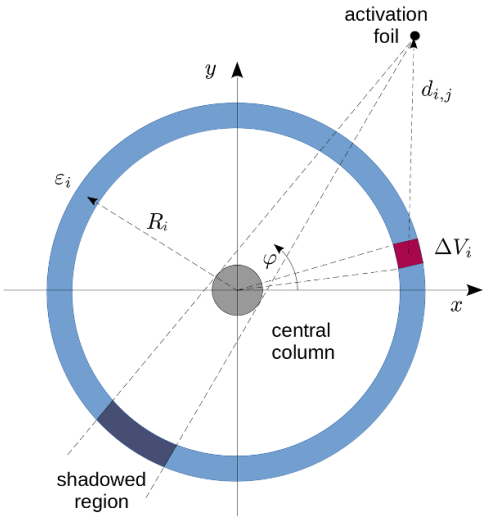

Figure 10. Geometry used to calculate the neutron flux at the activation foil (black circle) from the *i*th toroidal volume of emissivity ε_i (in light blue). The distance between each fractional volume ΔV_i (in purple) is $d_{i,j}$. The dark blue region does not contribute to the neutron flux at the activation foil as it is shadowed by the central column (light gray).

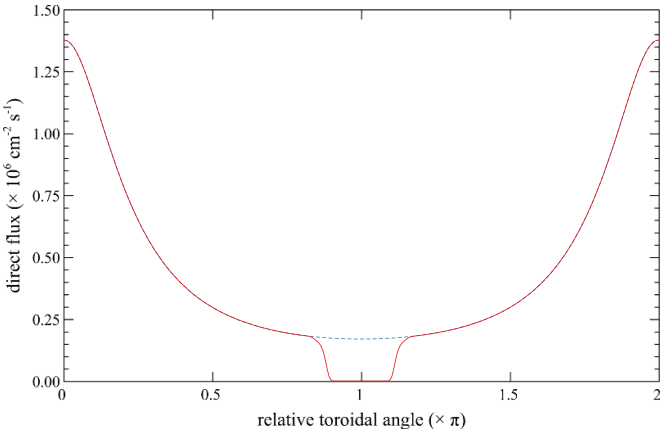

Figure 11. Direct flux at the activation foil as a function of the toroidal angle φ with and without the effect of the central column shadowing (red and dashed blue curves respectively). The toroidal location of the AF has been located arbitrarily at $\varphi = 0$.

where $n_i(t_m) = \varepsilon_i(t_m)\Delta V_i(t_m)$ is the rate of neutrons emitted isotropically by the fractional volume $\Delta V_i = V_i(t_m)/J$ over the entire solid angle and $S_{i,j}(t_m) = 4\pi d_{i,j}^2(t_m)$ is the surface of the sphere centered in $(R_i(t_m), Z_i(t_m), \varphi_j)$ at a distance $d_{i,j}$ from the AF. The effect of anisotropic neutron emission due to the dependence of the differential DD neutron production on the angle of emission is neglected here as its effect is to introduce variations less than 5% [36]. In equation (1), *i* refers to the 840 toroidal zones, of which figure 10 is a poloidal cross-section, on which the non-flux neutron emissivity is calculated. A top view of one such toroidal volume can be seen depicted in figure 10. The index $i = 1 \ldots I$ runs over all the toroidal volumes while the index $j = 1 \ldots J$ runs over the number J of fractional volumes ΔV_i in which each V_i is divided. Figure 10 shows the top view of the *i*-th toroidal volume (in blue) and the location of the AF (black dot): a fractional volume is shown in purple. The central column is also shown (light gray): the contribution to $\phi_{\mathrm{D},q}(t_m)$ from the fractional volumes that do not have a direct view of the AF (indicated in dark blue) is set to zero [37].

An MCNP simulation of the normalized F4 tally of mono-energetic neutrons through the central column was carried out and tallied in a 5 cm width on the other side. The neutron flux through the central column is attenuated by 99% for 2.5 MeV neutrons, and by 99.9% for 0.5 MeV neutrons.

The direct flux at the AF as a function of the toroidal angle is shown in figure 11 with and without the shadowing effect of the central column included. For each plasma discharge q, a single average direct neutron flux $\langle\phi_{\mathrm{D},q}\rangle = \sum_m \phi_{\mathrm{D},q}(t_m)/M$ is calculated from a set fluxes taken at M time slices throughout the flat-top period of the pulse duration. This was used for the calculation of the time averaged activation rate R in the foil for plasma discharge as:

$$R_q = \alpha_q \beta \Gamma_q V \sum_{k=1}^{K} \Phi_{\mathrm{T},q}(E_k)\,\Sigma(E_k) \tag{2}$$

where V is the AF volume, Γ_q the correction factor for the fast ion losses and redistribution, $\alpha_q = \langle\phi_{\mathrm{D},q}\rangle / \sum_k \Phi_{\mathrm{D},q}(E_k)$ converts the MCNP neutron flux spectrum into an absolute neutron flux and $\beta \approx 0.65$ corrects for the overestimate of the fast ion population in TRANSP/NUBEAM due to the guiding center approximation [24, 38]. This scaling factor, β, has been confirmed by recent measurements of proton prompt losses [39]. The terms in the sum include $\Sigma(E_k)$, the macroscopic cross-section determined from the microscopic cross-section of the $^{115}\mathrm{In}(n,n')^{115m}\mathrm{In}$ reaction from TENDL [40] multiplied by the number density on ^{115}In, and, $\Phi_{T,q}$, the total neutron fluxes per simulated neutron per discharge. The index k runs over the energy bins of 50 keV width centered in E_k in which the MCNP neutron flux spectra shown in figure 9 have been calculated. The neutron fluxes per simulated neutron Φ_{T} and Φ_{D} used in equation (2) are selected according to the NBI heating configuration for plasma discharge q.

The expression in equation (2) is based on the assumptions that the burn-up is negligible (correct to a very good approximation), the foil is so thin that the flux is not perturbed and that the neutron flux is constant: this is clearly incorrect as shown in figure 3, however, since the irradiation phase is much shorter than the half-life of the $^{115m}\mathrm{In} \rightarrow {}^{115}\mathrm{In} + \gamma$ decay the number of activated nuclei N is proportional to average value of the rate.

3.4. Expected number of γ-ray counts on the detector

During an experimental day, a sequence of Q irradiation and decay phases follow each other. The irradiation in each plasma discharge q lasts $\tau_q = t_{e,q} - t_{s,q}$ where the indexes 's' and 'e' indicate the start and end times of the NBI phase (for $q = 1$, $t_{s,1} = 0$). The number of activated radionuclides at the end of

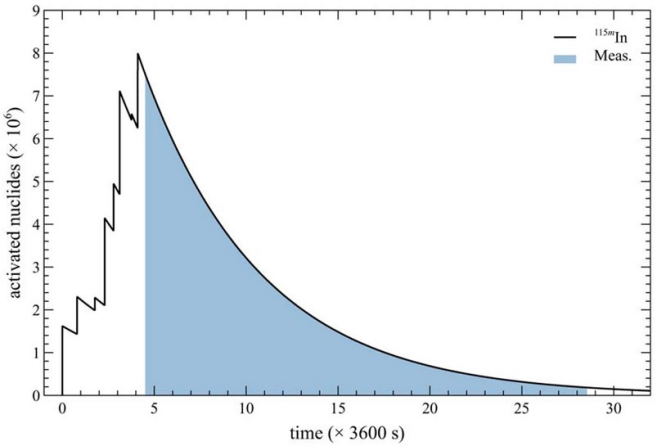

Figure 12. Time evolution of the activated radionuclides for the MU01 AF exposure on the 08 October 2021. The vertical steps indicate the activation for each plasma discharge. The blue area is the interval corresponding to the measurement time in which the expected number of decays is calculated.

the irradiation phase of pulse Q is given by:

$$N(t_{e,Q}) = \frac{R_Q}{\lambda}\left[1-\mathrm{e}^{-\lambda\tau_Q}\right] + \sum_{q=1}^{Q-1}\frac{R_q}{\lambda}\left[1-\mathrm{e}^{-\lambda\tau_q}\right]\mathrm{e}^{-\lambda(t_{e,Q}-t_{e,q})} \tag{3}$$

where λ is the decay constant of the $^{115m}\mathrm{In} \rightarrow {}^{115}\mathrm{In} + \gamma$ reaction and $N(t_{s,1}) = 0$. The shape of the activation over Q pulses defined in equation (3) is shown in figure 12. After this last pulse Q, the number of activated radionuclide decays according to:

$$N(t) = N(t_{e,Q})\,\mathrm{e}^{-\lambda(t-t_{e,Q})}. \tag{4}$$

The expected number of detected decays N_D in the γ-ray measurement time interval $\Delta t = t_2 - t_1$ following the last irradiation is then given by:

$$N_\mathrm{D} = \epsilon I_\gamma N(t_1)\left[1-\mathrm{e}^{-\lambda\Delta t}\right] \tag{5}$$

where ϵ is the γ-ray detector efficiency, and $I_\gamma = 0.46$ the branching ratio (γ-ray per disintegration). The expected number of detected decays N_D will be compared in the next section to the experimentally observed peak areas reported in table 1. The population of the ^{115m}In state due to energetic γ-rays from runaway electrons is not taken into account in this work. Observation of runaway electrons in MAST Upgrade is limited to plasma scenarios characterized by very low density not representative of the plasma scenarios of this study: in such plasmas, runaway electrons are emitted at the very end of the plasma discharge and thus of limited importance. In addition, the cross-section for the $^{115}\mathrm{In}(\gamma,\gamma')^{115m}\mathrm{In}$ reaction is approximately a factor 100 smaller than the one for the $^{115}\mathrm{In}(n,n')^{115m}\mathrm{In}$ and it has an energy threshold of 8 MeV.

Table 3. Comparison between the modeled N_D and the measured N_E counts on the γ-ray detector after irradiation of the AF for the selected experimental days.

Exp.	Date	N_E ($\times 10^5$)	N_D ($\times 10^5$)	ratio
MU01	20 August 2021	1.74 ± 0.001	2.24 ± 0.34	1.29 ± 0.20
MU02	26 January 2023	2.94 ± 0.013	3.45 ± 0.53	1.17 ± 0.18
MU02	27 January 2023	1.95 ± 0.001	2.43 ± 0.37	1.25 ± 0.19
MU03	20 October 2023	2.20 ± 0.001	1.91 ± 0.29	0.87 ± 0.13
MU03	27 October 2023	4.03 ± 0.020	4.61 ± 0.71	1.14 ± 0.17

3.5. Uncertainties in the modeling

The expected number of counts measured by the γ-ray detector calculated using equations (2)–(5) depends on several parameters and quantities whose uncertainties are reviewed in this section. To begin with, the following quantities are assumed to have negligible errors: the AF foil volume V, the decay constant λ and the branching ratio I_γ. The macroscopic cross-section Σ was calculated from the microscopic cross-section in the energy range of interest as determined in the TENDL database and the number density of ^{115}In. Σ has a relative uncertainty of approximately 3% in this energy range, determined from the variance provided by TENDL. The uncertainty associated with the unknown isotopic composition of the AFs has been estimated by varying the isotopic fraction of ^{115}In in the range 0.9 to 1.0 resulting in a variation of the macroscopic cross section of approximately 5%. The relative uncertainty in the integral total neutron flux from MCNP simulation is less than 2%. The relative uncertainty in the TRANSP/NUBEAM predicted direct neutron flux $\langle\phi_{\mathrm{D},q}\rangle$ in every simulation is the combination of a 10% relative uncertainty in the neutron emissivity $\varepsilon(t_m)$, due to the uncertainty in the kinetic profiles and in Z_eff, and the standard error of the average $\langle\phi_{\mathrm{D},q}\rangle$ for the qth plasma discharge. The uncertainty in the factor k is ± 0.05 as described in [24]. As a result, the overall relative uncertainty in α_q varies between 5% and 25% depending on the plasma discharge. Finally, the relative uncertainty in the detector efficiency is 8% (see section 2).

4. Results and discussion

Good agreement is found between modeled and experimental number of counts in the γ-ray detector for all the analyzed experimental days as shown in table 3 with the exception of the data for the 20 October 2023 due to unreliable Thomson Scattering kinetic profiles, leading to increased variance to the TRANSP simulations on that day. It is also interesting to note that the other prediction that deviates most from the measurements is for MU01 for which the energy fractions of the on-axis NBI had to be inferred from spectroscopic measurements (see section 3.1): the result here obtained suggests that the full energy component might have been slightly overestimated. Nevertheless, the best estimate of the ratio $N_\mathrm{D}/N_\mathrm{E}$ provided by the weighted average of the five measurements is 1.09 ± 0.075. The large uncertainty in N_D mainly reflects the uncertainties in the kinetic profiles input to TRANSP/NUBEAM and the large fluctuation of the neutron flux at the detector

in a single discharge. It is not possible to mitigate many of the uncertainties present in this work as they are inherent to the materials and diagnostics used, inherent qualities of a specific plasma discharge or the use of certain modeling codes. A potential cause for the slight over-estimation of this model is the lack of an accurate Z_{eff} profile for the TRANSP/NUBEAM simulations. The flat profile of $Z_{\text{eff}} = 1.5$ applied in this work is within the range commonly used in the community, but is likely not sufficiently high to correctly represent the impurities in the plasma. The addition of a new Z_{eff} measurement device on MAST-U would substantially increase the accuracy of accuracy of this model as well as the TRANSP simulations of MAST-U in general. The most critical parameters in this study are the isotopic composition of Indium foil and the the estimate of the reduction in the neutron emissivity due to the redistribution and loss of fast ions resulting from resonant and non-resonant perturbation. In order to eliminate these problems, it is suggested that future AF measurements should be carried out in dedicated experiments in which no or minimal magnetic perturbations are present and with an Indium foil of known isotopic composition. Luckily, this can be easily achieved in MAST Upgrade in L-mode plasmas in double null, conventional divertor configuration by using only the off-axis NBI as it has been shown that resonant perturbations are absent and non-resonant ones are very weak and do not affect the fast ions. Internal reconnection events, which cause massive ejection of fast ions from the plasma core with almost complete neutron production suppression, typically occur in the ramp-up phase or at the very beginning of the plasma current flat top phase and could be easily avoided by late NBI. An example of a suitable plasma discharge that matches the requirements above and that can be used as the reference scenario is shown in figure 13.

The measured magnetic perturbation with the Mirnov OMAHA coil is practically zero (compared with the 5th panel from bottom of figure 7) and the neutron rate measured by the FC (suitably scaled) matches the one predicted by TRANSP for the entire plasma discharge.

The agreement between N_{D} and N_{E} obtained with the forward modeling presented in this paper can then be used to absolutely calibrate the FC against the TRANSP/NUBEAM predicted neutron rate as well as to assess the validity of the kinetic profiles and the external auxiliary heating power in input to the models. These results support the idea that forward modeling of the AF can lead to an accurate estimate of the neutron yield and therefore potentially be used as a calibration procedure for ITER, DEMO and future fusion power plants as suggested in [41, 42]. In addition, for a fusion reactor, the reference plasma scenarios will be characterized by a neutron emissivity dominated by the thermal component from the DD and DT reactions thus simplifying significantly the forward modeling effort.

Data availability statement

All data that support the findings of this study are included within the article (and any supplementary files).

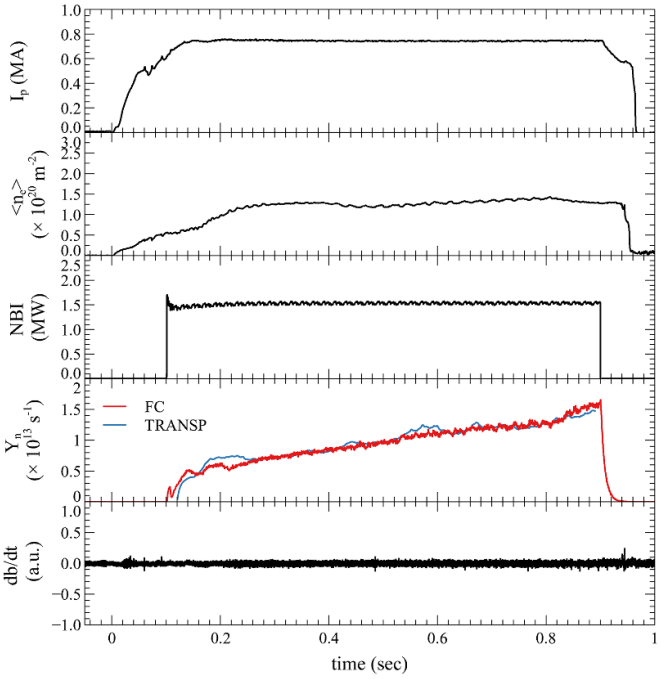

Figure 13. Example of a plasma discharge (# 47119) with off-axis NBI heating only ideal for activation foil measurements characterized by the lack of resonant and non-resonant perturbations causing the redistribution and loss of fast ions. The bottom panel of this figure can be compared with the 2nd panel from bottom of figure 7.

Acknowledgments

This work has been carried out within the framework of the EUROfusion Consortium, funded by the European Union via the Euratom Research and Training Programme (Grant Agreement No. 101052200 - EUROfusion). Views and opinions expressed are, however, those of the author(s) only and do not necessarily reflect those of the European Union or the European Commission. Neither the European Union nor the European Commission can be held responsible for them. This work has been carried out with the support of the RCUK Energy Programme (Grant No. EP/T012250/1) and of the Swedish Research Council (VR) Grant No. 2021-05485. This work has been funded by the EPSRC Energy Programme (Grant Number EP/W524426/1). Some sections of this work were part-funded by the EPSRC Energy Programme (Grant Number EP/W006839/1), to obtain further information on the data and models underlying this paper please contact PublicationsManager@ukaea.uk.

ORCID iDs

C L MacLean https://orcid.org/0009-0000-5927-7969
K Lennon https://orcid.org/0009-0005-2186-9754

References

[1] Hendel H W *et al* 1990 *Rev. Sci. Instrum.* **61** 1900–14
[2] Strachan J D *et al* 1990 *Rev. Sci. Instrum.* **61** 3501–4

[3] Nishitani T *et al* 1992 *Rev. Sci. Instrum.* **63** 5270–8
[4] Jassby D L *et al* 1995 *Rev. Sci. Instrum.* **66** 891–3
[5] Sasao M *et al* 2010 *Rev. Sci. Instrum.* **81** 10D329
[6] Nishio N *et al* 2011 *Plasma Fusion Res.* **6** 2405115
[7] Syme D *et al* 2014 *Fus. Eng. Des.* **89** 2766–75
[8] Batistoni P *et al* 2018 *Nucl. Fusion* **58** 026012
[9] Batistoni P *et al* 2018 *Nucl. Fusion* **58** 106016
[10] Snoj L *et al* 2012 *Fus. Eng. Design* **87** 1846–52
[11] Ishikawa M *et al* 2013 *Fus. Eng. Des.* **88** 1377–81
[12] Bertalot L *et al* 1999 *Rev. Sci. Instrum.* **70** 1137–40
[13] Chae S *et al* 2021 *Nucl. Eng. Technol.* **53** 3012–7
[14] Hoek M *et al* 1996 *Nucl. Instrum. Methods A* **368** 804–14
[15] Prokopowicz R *et al* 2011 *Nucl. Instrum. Methods A* **637** 119–27
[16] Stankunas G *et al* 2015 *Nucl. Instrum. Methods A* **788** 168–72
[17] Goldston R J *et al* 1981 *J. Comput. Phys* **43** 61
[18] Pankin A *et al* 2004 *Commun. Comput. Phys.* **159** 157
[19] Cecconello M *et al* 2018 *Rev. Sci. Instrum.* **89** 10I110
[20] Cecconello M *et al* 2023 *Plasma Phys. Control. Fusion* **65** 035013
[21] Bronson F L 2003 *J. Radioanal. Nucl. Chem.* **255** 137–41
[22] Goorley J T 2014 MCNP 6.1.1 Beta Release Notes Tech. Rep. LA-UR-14-24680 Los Alamos National Laboratory
[23] Stammers K and Loughlin M J 2006 *Nucl. Instrum. Methods Phys. Res. A* **562** 521–30
[24] Cecconello M *et al* 2019 *Nucl. Fusion* **59** 016006
[25] Appel L C *et al* 2006 *33rd EPS Conf. on Plasma Physics* p2.184
[26] Appel L C and Lupelli I 2018 *Comput. Phys. Commun.* **223** 1–17
[27] Conway N J *et al* 2010 *Rev. Sci. Instrum.* **81** 10D738
[28] Gibson K *et al* 2010 *Plasma Phys. Control. Fusion* **52** 124041
[29] Patel A, Carolan P, Conway N and Akers R 2004 *Rev. Sci. Instrum.* **75** 4944–50
[30] Knolker M, Osborne T, Belli E, Henderson S, Kirk A, Kogan L, Saarelma S and Snyder P 2021 *Nucl. Fusion* **61** 046041
[31] McClements K G *et al* 2012 *Phys. Plasmas* **19** 072514
[32] Turnyanskiy M, Challis C, Akers R, Cecconello M, Keeling D, Kirk A, Lake R, Pinches S, Sangaroon S and Wodniak I 2013 *Nucl. Fusion* **53** 053016
[33] Klimek I *et al* 2015 *Nucl. Fusion* **55** 023003
[34] Wu Y 2009 *Fusion Eng. Des.* **84** 1987–92
[35] Zankl G *et al* 1981 *Nucl. Instrum. Methods* **185** 321–9
[36] Wolle B *et al* 1999 *Nucl. Instrum. Methods A* **424** 561–8
[37] Batistoni P 2016 *Fusion Eng. Des.* **105** 58–69
[38] Sperduti A *et al* 2021 *Nucl. Fusion* **61** 016028
[39] Aboutalb A *et al* 2024 *Rev. Sci. Instrum.* **95** 083522
[40] Koning A J *et al* 2019 *Nucl. Data Sheets* **155** 1
[41] Cecconello M *et al* 2019 *Fus. Eng. Design* **146** 2049–52
[42] Cecconello M *et al* 2019 *J. Instrum.* **14** C09001